

## ARTICLE OPEN



# Two-dimensional single crystal monoclinic gallium telluride on silicon substrate via transformation of epitaxial hexagonal phase

Eugenio Zallo<sup>1✉</sup>, Andrea Pianetti<sup>2,7</sup>, Alexander S. Prikhodko<sup>3</sup>, Stefano Cecchi<sup>4</sup>, Yuliya S. Zaytseva<sup>3</sup>, Alessandro Giuliani<sup>5</sup>, Malte Kremser<sup>1</sup>, Nikolai I. Borgardt<sup>3</sup>, Jonathan J. Finley<sup>1</sup>, Fabrizio Arciprete<sup>2</sup>, Maurizia Palummo<sup>5</sup>, Olivia Pulci<sup>5</sup> and Raffaella Calarco<sup>6</sup>

Van der Waals (vdW) epitaxial growth of large-area and stable two-dimensional (2D) materials of high structural quality on crystalline substrates is crucial for the development of novel device technologies. 2D gallium monochalcogenides with low in-plane symmetry stand out among the layered semiconductor materials family for next-generation optoelectronic and energy conversion applications. Here, we demonstrate the formation of large-area, single crystal and optically active 2D monoclinic gallium telluride (m-GaTe) on silicon substrate via rapid thermal annealing induced phase transformation of vdW epitaxial metastable hexagonal gallium telluride (h-GaTe). Stabilization of multilayer h-GaTe on Si occurs due to the role of the first layer symmetry together with efficient GaTe surface passivation. Moreover, we show that the phase transformation of h-GaTe to m-GaTe is accompanied by the strain relaxation between Si substrate and GaTe. This work opens the way to the fabrication of single-crystal 2D anisotropic semiconductors on standard crystalline wafers that are difficult to be obtained by epitaxial methods.

npj 2D Materials and Applications (2023)7:19; <https://doi.org/10.1038/s41699-023-00390-4>

## INTRODUCTION

Two-dimensional (2D) layered materials such as post-transition metal chalcogenides (PTMCs)  $M_{III}-X$  ( $M_{III} = \text{In, Al, Ga}$  and  $X = \text{Se, Te, S}$ ) semiconductors are promising for electronic applications due to intriguing optical and vibrational properties<sup>1–4</sup>, including bandgap tunability from the IR to the UV spectral range and direct to indirect gap crossover as the number of layers decreases<sup>5,6</sup>, inverted sombrero like valence band dispersion for few layers<sup>7,8</sup>, and strong excitonic absorption<sup>9,10</sup>. Among these, GaTe exhibits two crystalline phases: a thermodynamically stable monoclinic (m-GaTe)<sup>11</sup> and a metastable hexagonal (h-GaTe)<sup>12</sup>, as shown by the bilayer (BL) stacking of Fig. 1a. Although the last one has a quasi-direct gap with promising thermoelectric applications<sup>13</sup>, the stable m-GaTe is attractive for the development of new generation optoelectronic devices due to its nonlinear optical response<sup>14,15</sup> and high photoresponsivity<sup>16,17</sup>. For potential fabrication of m-GaTe-based optical 2D devices it is important to form atomically thin single-crystal films on conventional semiconductors in controlled manner. Typically, ultra-thin 2D samples are obtained by exfoliation technique but often the photodetection results are spoiled due to fast reactivity of the material in ambient conditions and unintentional defects can be produced in the fabrication process<sup>18</sup>. Additionally, these approaches lack of scalability, controls of both thickness and interface formation, which are fundamental conditions for standard device production. Van der Waals (vdW)-type molecular beam epitaxy (MBE) can overcome these limitations due to the release of the lattice matching condition of conventional epitaxy by the growth of a 2D material

on another 2D or on passivated 3D materials<sup>19–21</sup>. On the other hand, recent growth advances show that high-quality and strain-free PTMCs are not yet available and pristine material information are still inaccessible due to the formation of Te oxide on the surface<sup>22</sup>. In particular, limited reports are available on MBE of InSe<sup>23</sup> and GaSe<sup>24,25</sup>, whereas GaTe materials are at an early stage of development<sup>26–28</sup>.

In this work, we demonstrate the formation of atomically sharp interface and single crystal m-GaTe on the silicon substrate with large-area coverage by using a two-step technique based on the phase transformation of h-GaTe. Firstly, metastable h-GaTe films have been grown on silicon via vdW-type MBE process. These epitaxial layers are protected from oxidation by in-situ encapsulation strategies. Secondly, the proposed rapid temperature annealing step of the h-GaTe film activates a phase transformation to strain-free single crystal 2D m-GaTe accompanied by the appearance of a pronounced photoluminescence (PL) peak. Grazing incidence diffraction (GID) and high-resolution transmission electron microscopy (HR-TEM) characterizations of the multilayer GaTe films down to a BL evidence the formation of the hexagonal phase after MBE process. Plan and cross-sectional HR-TEM observations unveil the atomic structure of the Si/GaTe interface and the crystallographic relationship between Si and GaTe films. Finally, both the electronic band structures and energetic stability of h-GaTe and m-GaTe layers on Si substrate have been studied by means of density functional theory (DFT) calculations as a function of film thickness explaining the crucial role of the substrate symmetry on the 2D GaTe growth. This work

<sup>1</sup>Walter-Schottky-Institut and TUM School of Natural Sciences, Technische Universität München, Am Coulombwall 4, 85748 Garching, Germany. <sup>2</sup>Dipartimento di Fisica, Università di Roma “Tor Vergata”, Via della Ricerca Scientifica 1, 00133 Rome, Italy. <sup>3</sup>Electron Microscopy Lab, National Research University of Electronic Technology (MIET), Zelenograd, 124498 Moscow, Russia. <sup>4</sup>Department of Materials Science, University of Milano-Bicocca, Via R. Cozzi 55, 20125 Milano, Italy. <sup>5</sup>Dipartimento di Fisica, Università di Roma “Tor Vergata”, and INFN, Via della Ricerca Scientifica 1, 00133 Rome, Italy. <sup>6</sup>Institute for Microelectronics and Microsystems (IMM), Consiglio nazionale delle ricerche (CNR), Via del Fosso del Cavaliere 100, 00133 Rome, Italy. <sup>7</sup>Present address: Department of Materials Science, University of Milano-Bicocca, Via R. Cozzi 55, 20125 Milano, Italy.

✉email: eugenio.zallo@wsi.tum.de

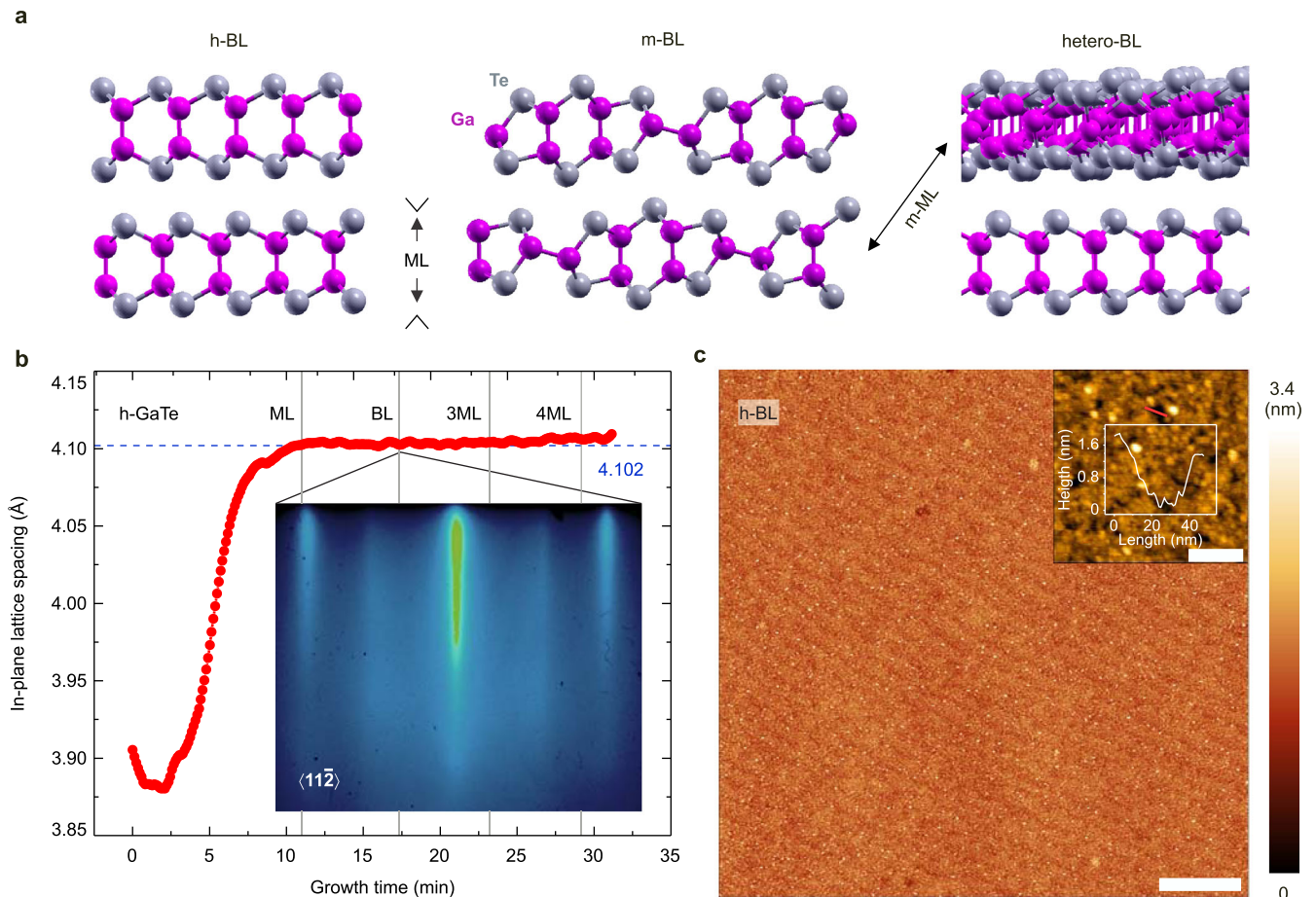


**Fig. 1** Van der Waals epitaxy of h-GaTe on Sb passivated Si(111). **a** Supercell bilayers (BLs) GaTe in the hexagonal phase with  $\beta$  stacking (h-GaTe) and monoclinic phase (m-GaTe), and vertical heterostructure by combining monolayers (MLs) of the two phases together (hetero-BL). **b** In-plane lattice spacing evolution as a function of time during the MBE growth. The lattice parameter is calculated from the streak distance in the in-situ RHEED patterns acquired perpendicular to the Si(11 $\bar{2}$ ) direction. The layer thickness dependency is obtained from the specular spot RHEED oscillations (see Supplementary Fig. 1). The inset shows the RHEED pattern from BL h-GaTe. **c** AFM height image of the BL h-GaTe measured after taking it out of the MBE chamber without capping layer. Scale bar is 2  $\mu$ m. The zoomed in AFM in the inset (scale bar is 100 nm) shows the profile highlighted in red of a discontinuity region in the GaTe layer.

highlights the great potential of activated phase transformation of MBE-grown metastable systems for the fabrication and study of high-quality stable 2D materials with in-plane low symmetry on standard semiconductors.

## RESULTS AND DISCUSSION

### Epitaxial layered hexagonal GaTe on silicon

The growth of GaTe on silicon is demonstrated in Fig. 1b, c. The Sb passivated Si(111) surface was prepared using the procedure described in Methods (see also previous works<sup>29–31</sup>). The in-situ reflection high-energy electron diffraction (RHEED) images were acquired perpendicular to the Si(11 $\bar{2}$ ) azimuth of the Si(111)-( $\sqrt{3} \times \sqrt{3}$ )R30°-Sb surface every 19 s, allowing to follow the evolution of the RHEED pattern as a function of deposition time. From the separation between the streaks we have determined the in-plane lattice spacing of the growing layer, using the RHEED pattern of the substrate as reference.

For an ideal 2D heteroepitaxy we expect that the first layer will adopt its unstrained lattice constant, as reported for the vdW epitaxy of graphene/hBN<sup>32</sup>, NbSe<sub>2</sub>/MoS<sub>2</sub><sup>19</sup>, TMDs/graphene<sup>33</sup>, group-IV monochalcogenides/graphene<sup>34</sup>, and 2D magnetic materials/graphene<sup>35</sup>. Figure 1b shows the almost rapid lattice relaxation ( $\sim 1$  monolayer, ML) from 3.9 Å of the substrate to 4.1 Å of the epitaxial layers due to the successful vdW epitaxy (we note

that a slow increase of the lattice constant to 4.12 Å is detected for the 11 ML GaTe after 80 min growth). We tentatively attribute the decrease of the lattice constant at the beginning of the growth to the formation of a cut half-sheet layer of GaTe<sup>36</sup>. After the first GaTe layer, the homoepitaxy proceeds with faster layer growth periods.

The narrow streaks from the RHEED pattern in the inset of Fig. 1b are the evidence of the 2D epitaxial growth of few layers GaTe. The weaker intermediate streaks arise from rotational domains and highlight the effective passivation of the Si surface (see also the GID characterization below and Supplementary Fig. 2). AFM revealed the formation of micrometer scale and homogeneous films, as shown in Fig. 1c by the typical topographic image of an uncapped BL GaTe measured immediately after the growth in order to limit the effect of the film oxidation. Interestingly, a careful observation evidences the presence of terraces with a period of  $\sim 220$  nm, which we attribute to the Sb passivated silicon substrate. The depth profile of discontinuity regions in the GaTe layer is reported in the inset of Fig. 1c: Thicknesses of  $\sim 0.85$  nm and  $\sim 1.7$  nm represent the size of ML and cell (stacking of two vdW layers or BL), respectively (see also Fig. 1a).

Further information about the crystalline phase and the domain alignment of the GaTe film are obtained by *ex situ* X-ray diffraction on a thicker film. Figure 2a depicts a conventional out-of-plane  $\omega - 2\theta$  scan, revealing two substrate reflections [i.e., Si(111) and

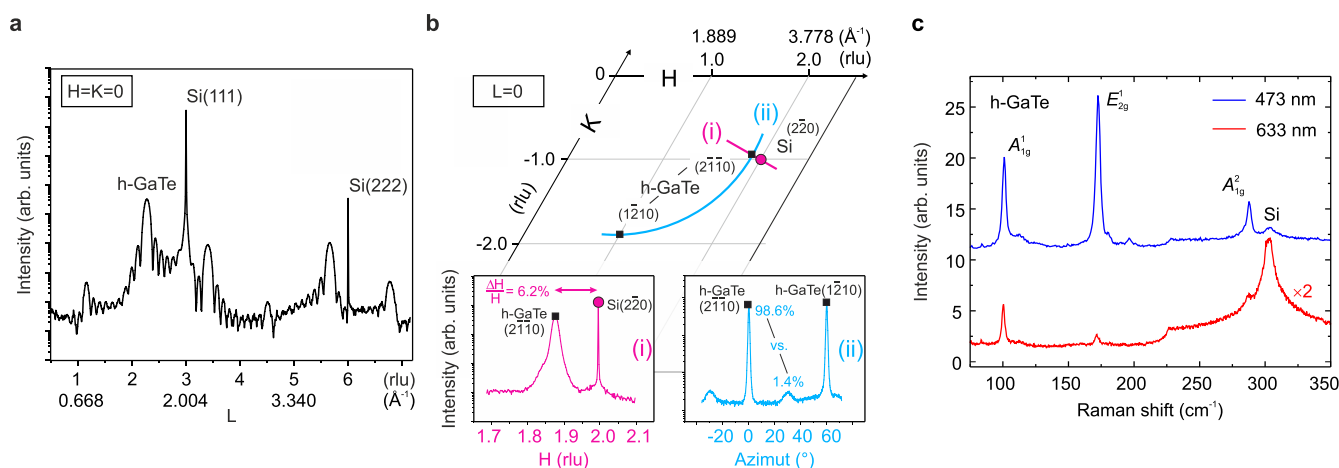


**Fig. 2** Synchrotron-based X-ray diffraction and Raman spectroscopy for 9 nm (11 ML) thick epitaxial h-GaTe film capped with ZnS/SiO<sub>2</sub>. **a** Symmetric out-of-plane  $\omega$ - $2\theta$  scan probing exclusively vertical lattice properties of the sample. The coordinates are given in reciprocal lattice units (rlu) and the corresponding absolute lengths of the scattering vector  $\mathbf{Q}$  in  $\text{\AA}^{-1}$ . **b** Area in reciprocal space at  $L = 0$  as accessible through GID. This refers exclusively to in-plane lattice properties. There are two scanning directions shown: (i) a radial scan along the GaTe[2 $\bar{1}\bar{1}$ 0] (magenta) and (ii) an azimuthal distribution (cyan) intersecting symmetrically equivalent GaTe peaks. **c** Raman spectra showing the main h-GaTe and the Si phonon modes with a 473 nm (blue) and a 632.8 nm (red) laser excitations.

Si(222)] as well as different orders of GaTe(000L) with  $L = 2n$  ( $n = 1-6$ ). The GaTe(000L) peak positions yield a vertical lattice parameter of 16.55  $\text{\AA}$ , which is in a good agreement with the theoretical prediction of 16.38  $\text{\AA}$  for the hexagonal phase<sup>12</sup>. Next to those layer reflections there are pronounced thickness oscillations separated by a  $\Delta l$  of 0.0714  $\text{\AA}^{-1}$  resulting in a layer thickness  $d = 2\pi/\Delta l$  of about 88  $\text{\AA}$ .

The GID geometry allows for the study of the in-plane lattice parameters of the layers<sup>37</sup>. Two relevant line profiles, as shown in Fig. 2b, are schematically highlighted within the plane of reciprocal space parallel to the sample surface: (i) The radial scan intersecting a Si(2 $\bar{2}$ 0) substrate reflection provides information about the in-plane orientation of the layer with GaTe[2 $\bar{1}\bar{1}$ 0] parallel to Si[ $\bar{1}\bar{1}$ 0], and the respective in-plane lattice parameter ( $\approx 6.2\%$  larger than the Si(220) net plane distance) which matches the RHEED values; (ii) The angular inspection of the GaTe[2 $\bar{1}\bar{1}$ 0] layer peak reveals a marked repetition every 60° but also a minor (1.4% vs. 98.6%) component 30° off. The sixfold rotational symmetry has been already observed for chalcogenide thin films grown on Si(111)<sup>38</sup> and it is the effect of the weak vdW coupling between the substrate and the epitaxial layer<sup>39</sup>.

Raman spectroscopy gives more insight into the symmetry of the GaTe layers (see Fig. 2c). Three main peaks are typically visible at 100.4, 172.1 and 287.3  $\text{cm}^{-1}$ . The number and position of the active modes resemble the configuration calculated in refs. 40,41 for h-GaTe with thicknesses between ML and bulk. Following this comparison, the modes are named as  $A_{1g}^1$ ,  $E_{2g}^1$  and  $A_{1g}^2$ , respectively. However,  $A_{1g}^2$  appears at much lower frequencies and no complete suppression of the  $A_{1g}^1$  and  $A_{1g}^2$  in the cross-polarized configuration (not shown) were found. We anticipate that misalignment of the sample, local strain fluctuations as well as crystal deformation in presence of the capping layer and Si substrate/Sb interface might affect the peak position (especially for the A modes) and the angular response. Blue laser excitation improves the signal-to-noise ratio and the relative variation of the peak intensity with excitation energy is possibly attributed to the different electron-phonon coupling for these modes<sup>42</sup>.

The microscopic analysis sheds light on the role of the substrate for the vdW epitaxy. The bright-field transmission electron microscopy (TEM) image of h-GaTe on Si(111) substrate plan-view specimen in Fig. 3a (zoomed fragment in Fig. 3b) shows moiré pattern with periodicity close to 2.9 nm, due to lattice

mismatch between h-GaTe and Si. It can be seen that h-GaTe forms on the Si surface as triangular-shaped grains of  $\sim 20-80$  nm in size. The diffraction pattern presented in Fig. 3c matches very well on the local scale with the GID results obtained in Fig. 2: Si{220} and GaTe{11 $\bar{2}$ 0} reflections are observed with the same symmetry and h-GaTe grains on Si are almost not rotated with a mosaicity of 2°. Supposedly, such mosaicity is caused by the tendency of h-GaTe to minimize strains arising from its lattice mismatch with Si substrate. Similar grain rotations have been recently studied for the GeSbTe layer grown on Si(111)-( $\sqrt{3} \times \sqrt{3}$ )R30°-Sb substrate with a mosaicity of 4°<sup>43</sup>. We assume that the larger mosaicity in the case of GeSbTe is caused by a larger lattice mismatch between GeSbTe and Si.

In addition, the cross-sectional HR-TEM image of Fig. 3d highlights a sharp interface between h-GaTe and Si. Remarkably, misfit dislocations are visible resulting from the alignment of not rotated h-GaTe grains with the Si substrate. Two misfit dislocations are visualized via geometric phase analysis (GPA, see Supplementary Fig. 3)<sup>44</sup> and marked by numbers 1 and 2. The distance between the dislocations closed to 2.9 nm is determined by the lattice mismatch between Si and h-GaTe. Figure 3e demonstrates  $\epsilon_{xx}$  component of strain field around dislocation 2: The strains are negative and compressive on the Si side (where an extra half-plane should be considered), whereas positive and tensile strains are expected on the other side and the largest strain values occur in the immediate core region. By drawing a Burgers circuit surrounding the misfit dislocation core, as shown by the dashed line in Fig. 3d, the Burgers vector is determined as  $b = a/4[1\bar{1}0]$ , where  $a$  is the lattice constant of Si.

For a complete picture of the material under study, we report in Fig. 4a, c the electronic band structures for the h-GaTe in the bulk and BLs forms, respectively. Both gaps are indirect with the conduction-band minimum (CBM) located at the M point and the valence-band maximum (VBM) at the  $\Gamma$  point for the bulk and near the  $\Gamma$  point for the BL (where a typical inverted sombrero shape of last occupied states appears, see Supplementary Fig. 5). As a consequence, no PL emission is measured from bulk like h-GaTe, as shown by the gray line in Fig. 5b, where a bump around 550 nm (2.25 eV) is ascribed to recombination in the Si substrate<sup>45</sup>. The same behaviour is found in h-GaTe for thinner layers (not shown). Finally, the structural and optical data demonstrate the fabrication by MBE of multilayers GaTe in a highly ordered hexagonal phase

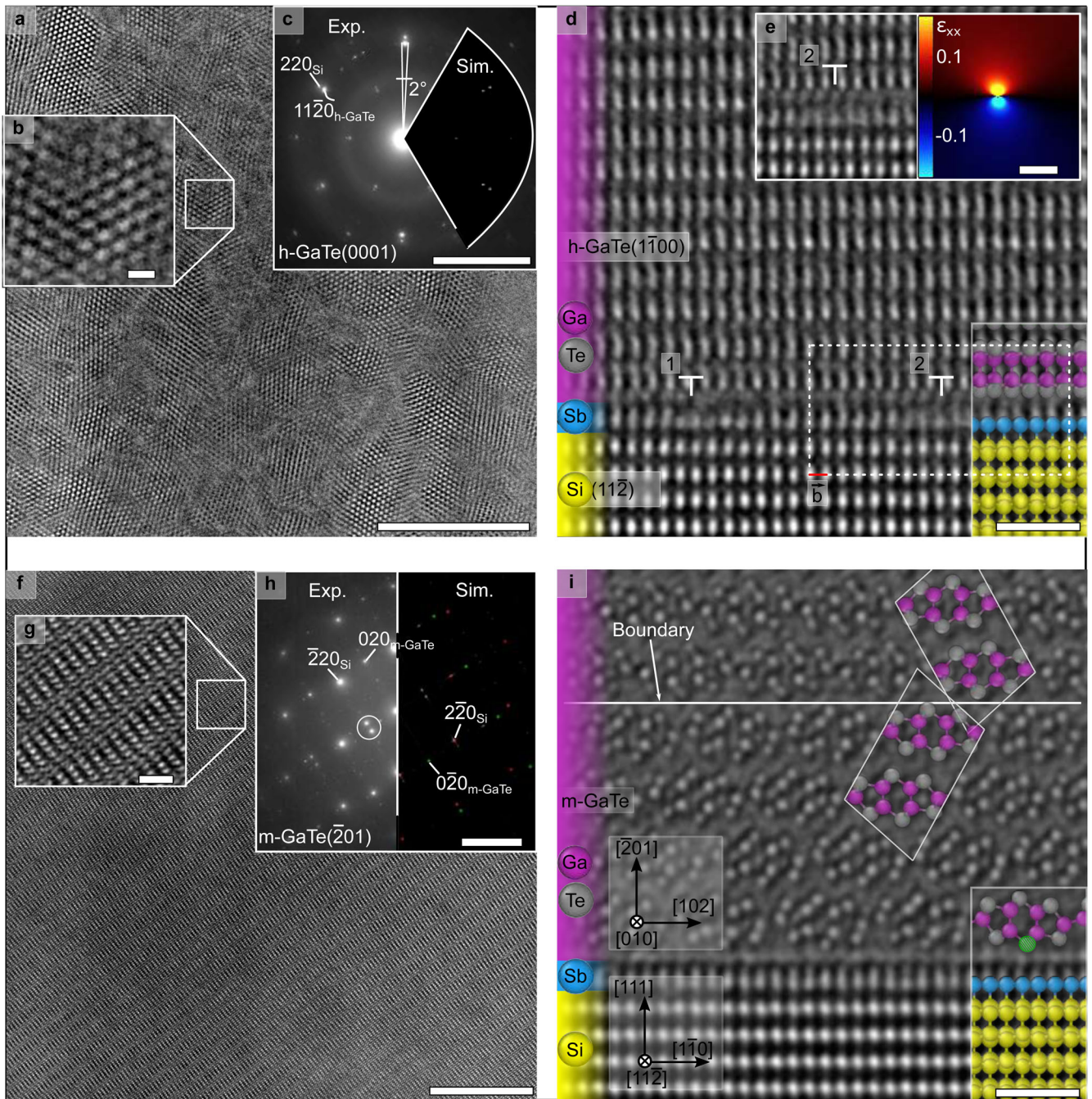


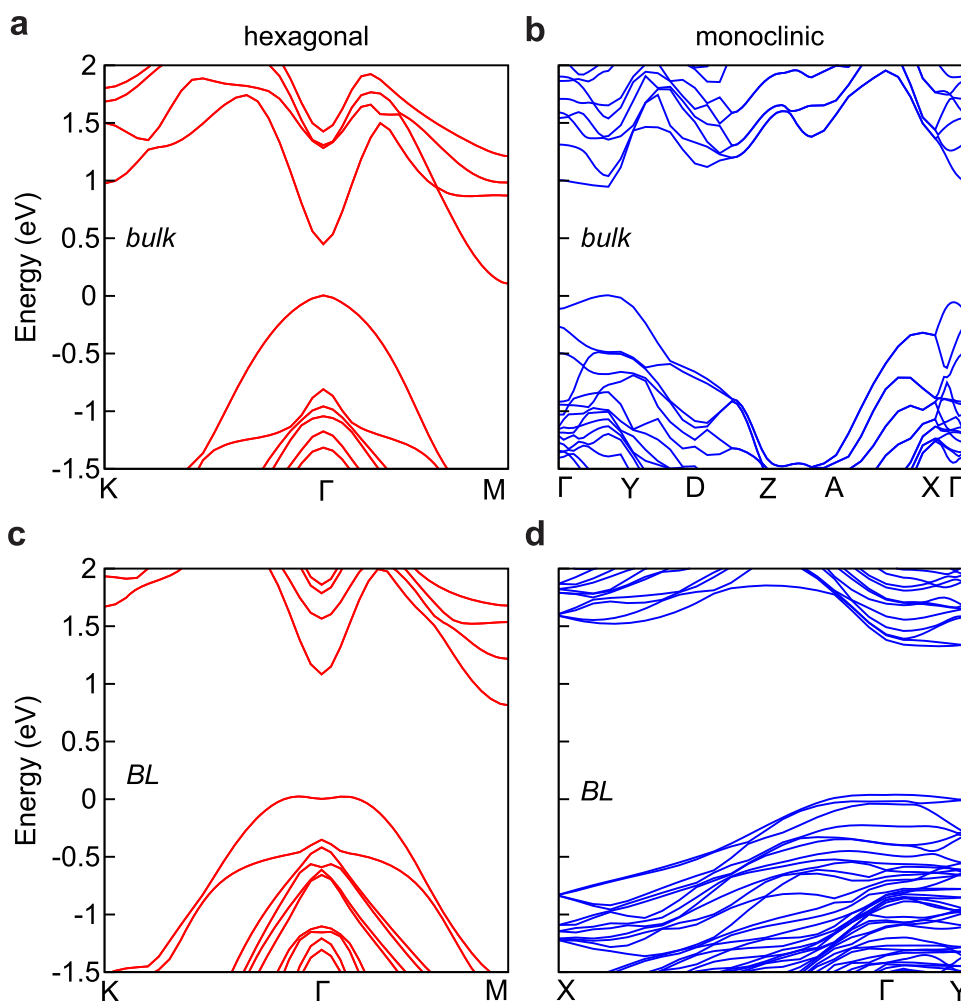
**Fig. 3** Electron microscopy studies of as-grown h-GaTe and m-GaTe on Si. **a, f** Bright field plan-view micrograph of as-grown h-GaTe and m-GaTe (h-GaTe after RTA annealing). The scale bar is 100 nm and 10 nm, respectively. The insets (**b, g**) show zoomed fragments (scale bar is 5 nm and 1 nm, respectively) and (**c, h**) diffraction patterns obtained along Si(111) (scale bar is  $5 \text{ nm}^{-1}$ ). **d, i** Cross sectional high-resolution (HR)-TEM image of as-grown Si/h-GaTe and Si/m-GaTe interfaces and near interface regions, respectively (scale bar is 1 nm). Panel (**d**) illustrates the misfit dislocations arisen at the interface between Si(112) and nonrotated h-GaTe(1 $\bar{1}$ 00). **e**  $\epsilon_{xx}$  component of the strain field around the misfit dislocation core. The color scale indicates strain changes of  $-20\%$  to  $20\%$  (scale bar is 0.5 nm). Panel (**i**) shows the codirection of m-GaTe[020] and Si[112] with “twin-like” boundary highlighted by white solid line.

and the absence of compositional disorder with no monoclinic phase present in the layers.

### Phase transformation to single crystalline monoclinic GaTe

For the potential application of GaTe as optical active material a strategy to obtain high-quality m-GaTe on Si is essential. In the following, we consider the formation of h-GaTe as an intermediate step and we use a thermal treatment of the multilayer h-GaTe to

activate a phase transformation between the metastable h-GaTe and the stable m-GaTe. GaTe is a very reactive material but the procedure of capping the as-grown layers efficiently protects the surface from oxidation, as demonstrated by the preserved Raman scattering even after two years from the first measurement (see Supplementary Fig. 6). For this experiment, the layers were capped with  $\text{Si}_3\text{N}_4$ , which is thermally stable<sup>46</sup> and the annealing temperature was  $550^\circ\text{C}$  for a duration of 30 min.



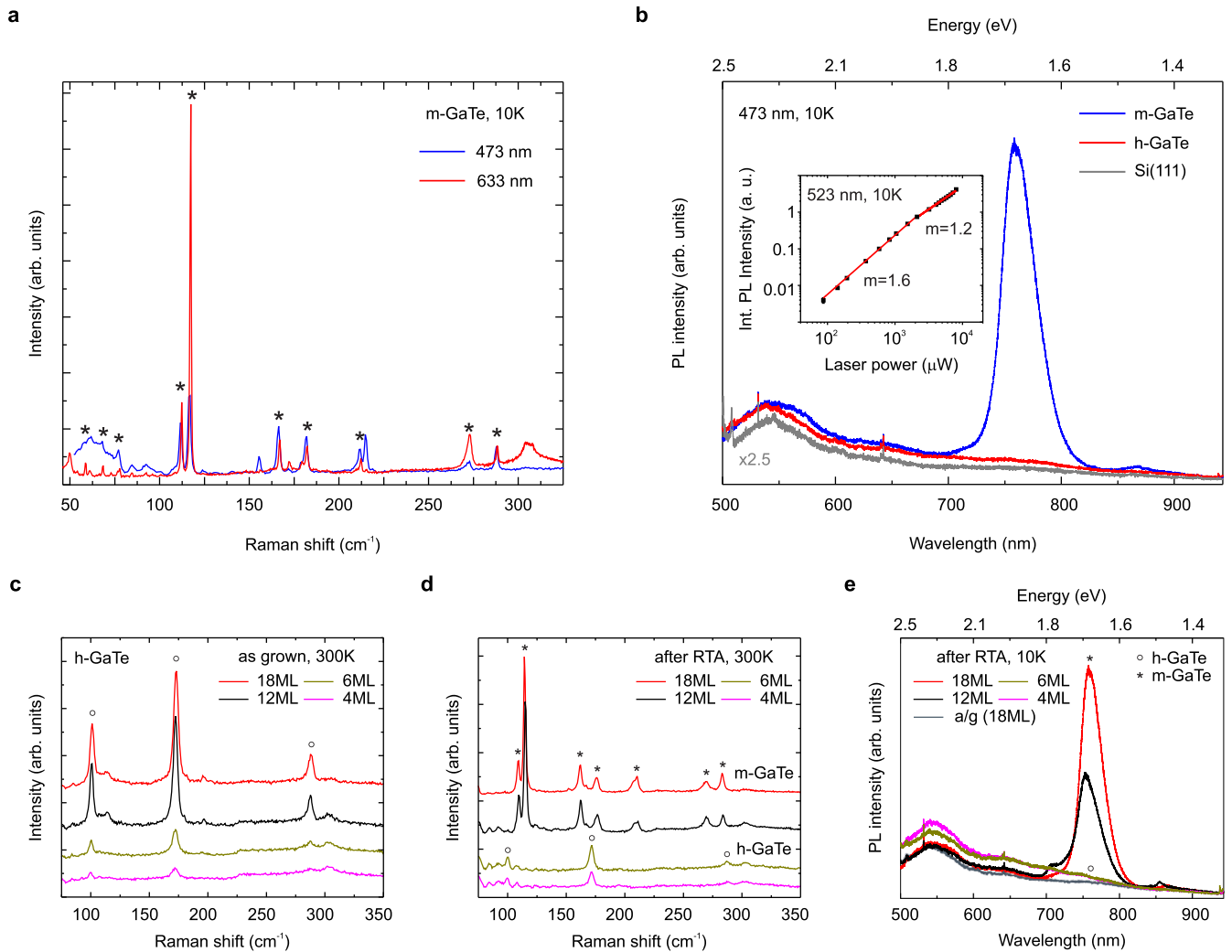
**Fig. 4** Electronic band structures in GaTe. DFT band structures of h-GaTe (a, c) and m-GaTe (b, d) bulk and BL, respectively. For more details about the Brillouin zones and  $k$ -paths used see the Supplementary Fig. 4.

Figure 5a represents the Raman spectrum after rapid thermal annealing (RTA) of 18 ML h-GaTe. Both mode positions and numbers are in very well agreement with the m-GaTe crystal structure, as reported in ref. <sup>14</sup>. Differently to exfoliation<sup>14,16,47</sup> and physical vapour deposition methods<sup>15,22</sup>, the full width at half maximum (FWHM) of the two principal modes at 112.2 and 117.3  $\text{cm}^{-1}$  (0.9 and 0.8  $\text{cm}^{-1}$ , respectively, excited with red laser) suggest a very high crystalline quality and no Te oxidation has been detected<sup>48</sup>. The crystal alignment is also confirmed by the X-ray diffraction (XRD) pattern where a lattice periodicity of 7.4  $\text{\AA}^{-1}$  with the (210) $n$  planes oriented parallel to the vdW gaps (along the Si(111)) were measured (see Supplementary Fig. 7).

Importantly, bright-field TEM image of the plan-view specimen of m-GaTe on Si shows m-GaTe layer without the presence of any grains (see Fig. 3f). The zoomed fragment of Fig. 3g evidences the contrast features similar to moiré pattern caused by overlapping m-GaTe and Si crystals along the electron beam direction. This produces rows of  $\approx 6$  bright spots that are periodically interleaved within the stripe boundary ( $\approx 1.5$  nm in width). The period of rows is shifted relatively to each other in the neighbour stripes due to the formation of “twin-like” diffraction spots marked by white circle in Fig. 3h. In addition, the alignment between m-GaTe and Si lattices is shown by the codirection of m-GaTe[020] and Si[11 $\bar{2}$ ]. In order to elucidate the diffraction pattern, we have performed simulation of the diffraction process using multislice algorithm applied to the built atomistic model<sup>49</sup>. This model contains m-

GaTe[ $\bar{2}01$ ] layers with vdW gaps parallel to the interface placed upon the Si[111] substrate and both layers are 15 nm thick. The topmost Si bilayer is replaced by Sb atoms in accordance with the Si(111)-( $\sqrt{3} \times \sqrt{3}$ )R30° surface reconstruction and the electron wave propagates along the Si[111] direction. Precise matching between experimental and simulated patterns reveals the correctness of the created model presented in the right corner of Fig. 3i. The spots of the diffraction pattern are caused by the double diffraction process (see details in the Supplementary Fig. 8). By using a selective aperture with a diameter of 650 nm, we obtain equivalent diffraction patterns in regions several microns apart, which is the evidence of the presence in the layer of sub-micrometer sized m-GaTe monocrystalline grains. Additionally, dark-field imaging mode of 020 m-GaTe diffraction spot allows us to visualize the m-GaTe layer as a bright region with the size of several micrometers (see Supplementary Figs. 9, 10). Within this region, 020 m-GaTe planes have the same orientation with respect to the Si substrate. To the best of our knowledge this is the highest quality layered m-GaTe observed so far already integrated on silicon.

The presence of the monoclinic layers close to the interface with the Si substrate separated by vdW gaps is well shown by the cross-sectional HR-TEM of Fig. 3i, where a perfect agreement with Ga and Te atomic positions reported in Fig. 1a is found. The Si/m-GaTe interface is sharp and matching between Si and m-GaTe lattices occurs without the presence of any strains, as shown by



**Fig. 5** **h-GaTe to m-GaTe phase transformation and phase stability as a function of film thickness.** **a** Low-temperature Raman spectra of 18 ML h-GaTe transformed into m-GaTe after RTA at 550°C for 30 min. The laser excitations are 473 nm and 632.8 nm. **b** Low-temperature PL spectra from Si substrate (gray), 18 ML GaTe in the as-grown h-GaTe (red) and m-GaTe after RTA (blue). The inset shows the power dependence of the PL peak at 1.635 eV measured with 532 nm laser excitation wavelength at 10 K with superlinear slope ( $m$ ) of the excitonic recombination and saturation of the defect-related channel at higher power. **c**, **d** Raman spectra of h-GaTe as-grown and after RTA, respectively, for 4, 6, 12, 18 layers. The vibrational modes from h-GaTe and m-GaTe are highlighted with circles and stars, respectively. **e** Low-temperature PL spectra of h-GaTe films after RTA compared with the as-grown (a/g) 18 ML h-GaTe. Both Raman and PL are excited with 473 nm laser. In order to preserve the material integrity and to protect it from oxidation, all the samples have been capped with  $\text{Si}_3\text{N}_4$  before annealing.

the  $\epsilon_{xx}$  obtained via GPA analysis (see Supplementary Fig. 11). It should be noted that m-GaTe layers close to the interface can be rotated by  $180^\circ$  around m-GaTe[201], as shown for two m-GaTe unit cells in the upper part of Fig. 3i. In contrast to the Si/h-GaTe interface, where the lowest Te atoms have the same position with respect to the substrate, this distance varies in Si/m-GaTe depending on the Te position within the unit cell (see Supplementary Fig. 12). Since every third Te atom is closer to the substrate than the others (see the shaded green atom at the lower right corner of Fig. 3i), we can attribute the formation of quite large monocrystalline m-GaTe grains to the lower vdW interactions between Te and Sb atoms leading to more separation to the substrate. Moreover, the Si/h-GaTe interface showed misfit dislocations due to interplanar distance mismatch between parallel arranged h-GaTe(1120) onto Si(220) planes. Differently, in the case of m-GaTe on Si, the matched m-GaTe(404) are tilted with respect to the Si(220) atomic planes by approximately  $4.7^\circ$  without any appearance of misfit dislocation (see Supplementary

Fig. 13). This denotes that besides the minimized influence of the substrate lattice on the film, due to the Sb passivation, and the special atomic arrangement at the Si/m-GaTe interface, the tilt of the m-GaTe atomic planes eliminates the mismatch at the Si/m-GaTe interface leading to the absence of strains, as demonstrated using the GPA analysis.

Finally, the monocrystalline structure is accompanied by PL emission at 758.4 nm (1.635 eV, see Fig. 5b), which is the main signature of the successful transformation to m-GaTe<sup>50</sup>. Power dependence analysis of the PL peak reveals excitonic transition competing with another possibly defect-related decay channel<sup>51</sup>, which appears to be saturated at higher excitation power densities (see the inset of Fig. 5b).

DFT calculations show that bulk m-GaTe has a direct band gap near the Y point of  $\sim 1$  eV with a larger quasi-direct gap along  $\Gamma$ -Y for BL m-GaTe (m-BL), as reported in Fig. 4b, d, respectively. The almost flat parallel bands predicted by calculation suggests the presence of an intense PL with excitonic nature, which will

**Table 1.** Energetic stability of monolayer (ML) and bilayer (BL) GaTe with respect to the corresponding structure in the hexagonal  $\beta$  form whose ground state total energy is set to zero.

Geometry ML	E (meV/atom)	Geometry BL	E (meV/atom)
h-ML $\beta$	0	h-BL $\beta$	0
h-ML G2	+3	h-BL G2	+2.3
		h-BL $\epsilon$	-0.4
m-ML	+1.3	m-BL	-2.3
		hetero-BL	+8

deserve further investigations both at the theoretical and experimental level. Interestingly, m-BL band dispersion is similar to the ML m-GaTe (m-ML) case already discussed in the literature<sup>52</sup>, but with a stronger flat nature of the VBM.

### Phase stability of layered GaTe

Important information about the phase stability of GaTe can be acquired by looking at the optical response as a function of layer thickness, as reported in Fig. 5c–e. For the as-grown material, three main Raman modes are visible with decreased intensity as the volume of the material probed is reduced<sup>53</sup>. Raman and PL spectra after RTA are shown in Fig. 5d, e, respectively. The 12 ML thick GaTe is optically active with PL peak blue shifted to 1.644 eV and Raman modes almost unshifted with respect to the 18 ML film. This is consistent with the theoretical calculations where direct band transition is found down to the BL m-GaTe (see Fig. 4d). Surprisingly, both the 4 ML and 6 ML cases show Raman and PL spectra similar to as-grown h-GaTe. These layer thicknesses exceed the thermodynamic prediction of 1.27 ML reported by Zhao et al. for the critical value for phase transformation to m-GaTe<sup>54</sup>.

In order to clarify this point, the impact of the starting epitaxial layer on the energy stability of the second layer was calculated. Table 1 reports the total energy of the various structures, taking as zero the hexagonal structure in the  $\beta$  stacking configuration. Both ML and BL with G2 stacking, discussed in ref. 55, were also simulated, resulting always less stable than the  $\beta$  stacking and the m-ML. For the sake of completeness, the total energy of the BL h-GaTe (h-BL) with  $\epsilon$  stacking, proposed to be present in the few-layer samples, has been calculated with values very similar to the  $\beta$  stacking. Even though the m-BL is the energetically preferred configuration, the h-BL becomes more favourable when the first layer is in the hexagonal form with respect to that of a second monoclinic layer (hetero-BL), as observed in the experiments. This finding highlights the role of the crystal symmetry in vdW epitaxy for the phase stabilization<sup>56,57</sup>. Therefore, we can define two growth regimes for thicknesses  $\leq 6$  ML, where h-GaTe is stable, and  $> 6$  ML, where the effect of the first layer is weaker and GaTe relaxes in the monoclinic phase after RTA process. It is worth to point out that the use of a fully passivated Si(111) substrate with threefold symmetry is fundamental to allow the vdW epitaxy of an almost unstrained h-GaTe already in the ML form and it clearly supports the stabilization of this phase with respect to the monoclinic one. As the growth proceeds, additional energy is accumulated at the grain boundaries, typical of the triangular-shaped grain-like structure from h-GaTe (see Fig. 3a), resulting in a more preferable transformation of h-GaTe into m-GaTe after RTA process. Moreover, our results suggest that the change of the growth kinetics and wetting condition for thicker layers<sup>58</sup>, which are visualized by an enhanced vertical growth giving rise to stepped surfaces (see Supplementary Fig. 14), might play a crucial role to determine the thickness where the monoclinic phase

becomes favored. We leave to future investigations a complete clarification of this aspect.

In conclusion, the vdW epitaxy of metastable h-GaTe on silicon down to BL was realized by means of MBE. A complete structural and morphological characterization demonstrate the large-area coverage and high crystalline quality of the films in the hexagonal phase with tenths nm-sized grain-like structure. Phase transformation of h-GaTe to grain boundary-free m-GaTe with pronounced PL was activated by thermal annealing in the nitrogen atmosphere of the 18 ML and 12 ML films while the h-GaTe structure was stabilized up to at least 6 ML. Such phase transition mechanism was accompanied by strain relaxation at the interface between the Si substrate and m-GaTe. The extended stability of the thinner h-GaTe layers is explained in terms of energetics when the vdW epitaxy starts on a material with hexagonal symmetry. Moreover, DFT calculations show that the bandgap of the bulk m-GaTe (h-GaTe) increases at very small thickness but does not change its direct (indirect) nature. Our studies show that the high crystalline quality, scalable and silicon-integrated m-GaTe may be a key ingredient for next-generation quantum and optoelectronic devices. Finally, the control of unstable phases of matter makes novel thin layer-based multifunctional systems now available by combining the two complementary GaTe phases with TMDs, h-BN or 2D magnetic materials.

## METHODS

### Molecular beam epitaxy

The GaTe films with thicknesses between 1.5 and 15.5 nm (from 2 to 18 MLs, where 1 ML = 0.85 nm is a complete assembly of Te/Ga/Ga/Te slabs enclosed by two vdW gaps) were grown by solid-source MBE on Sb passivated Si(111)-( $\sqrt{3} \times \sqrt{3}$ )R30° surfaces with 0.03° miscut. After standard silicon cleaning, the Si(111)-(7 × 7) reconstruction was obtained by heating up the substrates to 720°C at a rate of 0.2°C for 5 min. Subsequently the surfaces were exposed to a Sb flux for 5 min and cooled down to 650°C at a rate of 0.3°C. After 5 more minutes, the temperature is cooled down to 300°C at the same rate and annealed for 3 min before the Sb shutter was closed. The substrate temperature was 375°C for all the growths. RHEED technique was used for confirming the formation of the Si(111)-(7 × 7) reconstruction prior the Sb termination of the substrate (see Supplementary Fig. 15) and for monitoring the vdW epitaxy. Due to the high reactivity of the GaTe surface in the ambient environment, the films were capped by sputtering in the load lock with ~30 nm thick ZnS/SiO<sub>2</sub> or Si<sub>3</sub>N<sub>4</sub> amorphous layers after sample cooling to room temperature and before taking it out of the MBE chamber.

### Atomic force microscopy

Tapping mode atomic force microscopy (AFM, Veeco Nanoscope III) was employed to probe the surface morphology.

### Transmission electron microscopy

HR-TEM studies of 15 nm thick h-GaTe and m-GaTe layers grown on Si(111) substrate were carried out in a FEI Titan Themis 80-200 TEM operated at 200 kV and equipped with spherical aberration image corrector, FEI Ceta 16M complementary metal-oxide-semiconductor (CMOS) camera, and Super-X EDX detector. Cross-sectional HR-TEM images were obtained with  $C_s$  value close to 0.5  $\mu\text{m}$  and with a bit overfocused objective lens leading to atomic columns visualization as bright spots in the images in case of thin enough TEM specimens. In order to reduce noise in HR-TEM images we used Wiener filter developed in ref. 59, which is implemented as a plug-in in Digital Micrograph software by Gatan Inc. Graphic phase analysis<sup>44</sup> of the cross-sectional HR-TEM images was performed via Strain++ software<sup>60</sup> for obtaining 2D strain

fields at the near interface regions between the Si substrate and epitaxial layer. 2D  $\epsilon_{xx}$  around the misfit dislocation cores was obtained by carrying out GPA analysis by using non-colinear reciprocal lattice vectors Si(111) and Si(220), mask diameter of  $2 \text{ nm}^{-1}$  and Si substrate as a reference region. Atomic positions were visualized via OVITO software<sup>61</sup>. Plan-view and cross-sectional TEM specimens were prepared by a focused ion beam technique in a dual-beam workstation Helios NanoLab 650.

### X-ray diffraction

In order to probe lattice properties along growth direction as well as within the GaTe layers, we used, respectively, synchrotron-based coplanar XRD and GID. The GID experiments were performed at the PHARAO beamline at the U125/2-KMC (BESSYII, Helmholtz-Zentrum Berlin) using an X-ray energy of 10 keV. The layer thicknesses were estimated by high-resolution XRD and X-ray reflectivity (XRR) by a four-circle PANalytical X'Pert Pro Materials Research diffractometer equipped with a Ge(220) hybrid monochromator and Cu  $K\alpha_1$  ( $\lambda = 1.540598 \text{ \AA}$ ) X-ray radiation. For  $\omega$ - $2\theta$  scans, a 1 mm slit at the detector side was used. The data analysis was carried out using X-ray utilities<sup>62</sup>.

### Raman and PL spectroscopies

Micro-Raman measurements were conducted in backscattering geometry by means of a continuous wave laser with excitation wavelengths in the visible (473 nm, 632.8 nm) at room temperature and 10K (1  $\mu\text{m}$  diameter spot). The character of the vibrational modes was assigned by means of polarization-resolved spectroscopy.

PL measurements were carried out using a liquid-He flow cryostat at 10K with 473 nm and 532 nm lasers focused to a diameter of 1  $\mu\text{m}$ .

### Rapid thermal annealing

The phase transformation of the as-grown GaTe was activated in a RTA furnace JetFirst100 under 1 bar nitrogen atmosphere at 550°C for 30 min. The annealing (cooling) ramp rate was 40°C/s (1°C/s).

### DFT calculations

The structural optimizations and electronic structures are obtained by DFT calculations performed with the Quantum-Espresso code<sup>63</sup> and using the Perdew-Burke-Ernzerhof (PBE) functional<sup>64</sup>. vdW corrections are applied on top of the PBE functional in order to take into account the weak interaction between the layers<sup>65</sup>. Scalar-relativistic optimized norm-conserving Vanderbilt pseudopotentials from the PseudoDojo repository (v0.4) are used with a plane-wave cutoff of 160 Ry for structural optimization and total energy calculations<sup>66,67</sup>. Spin-orbit correction are taken into account for the electronic band calculations. A careful convergence with k-point meshes is performed, shifted grids of  $16 \times 16 \times 1$  and  $8 \times 16 \times 1$  for h-GaTe and m-GaTe give errors in the total energy smaller than 1 meV. The crystal structures (see Fig. 1a) both in the hexagonal ( $\beta$  stacking, where Te atoms of a GaTe layer are aligned with the Ga atoms of the adjacent layers, along the z-direction) and monoclinic phases are obtained by fully relaxing the atomic positions that are available for the two bulk phases<sup>68</sup>. In order to simulate isolated MLs and BLs, we use a supercell size of 41  $\text{\AA}$  in the z-direction. To determine if the deposition of a monoclinic layer on top of a first deposited h-GaTe ML (h-ML) can be energetically favoured with respect to the deposition of another hexagonal layer, we build up a supercell for an hetero-BL, by combining the two unit cells with the CellMatch python code<sup>69</sup> and to be consistent with the experimental observation, we leave the h-ML practically unstrained. The supercell contains 452 atoms (see Fig. 1a) and a very small compressive strain on the monoclinic layer of about 4‰ is

present. For such large cell we use ultrasoft pseudopotentials and at the  $\Gamma$  point only k-space sampling with a kinetic energy cutoff of 60 Ry and 360 Ry for the charge density. Then, in order to compare energetically the h-BL and hetero-BL structural models, we use the same computational setup to simulate also the corresponding h-BL ( $\beta$ ) supercell, containing 472 atoms.

### DATA AVAILABILITY

The data that support the findings of this study are available from the corresponding author upon reasonable request.

Received: 21 September 2022; Accepted: 10 March 2023;

Published online: 27 March 2023

### REFERENCES

1. Gong, C. & Zhang, X. Two-dimensional magnetic crystals and emergent heterostructure devices. *Science* **363**, 4450 (2019).
2. Cai, H. et al. Synthesis and emerging properties of 2D layered III-VI metal chalcogenides. *Appl. Phys. Rev.* **6**, 041312 (2019).
3. Attaccalite, C., Palumbo, M., Cannuccia, E. & Grüning, M. Second-harmonic generation in single-layer monochalcogenides: A response from first-principles real-time simulations. *Phys. Rev. Materials* **3**, 074003 (2019).
4. Bejani, M. et al. Lattice vibrations and electronic properties of GaSe nanosheets from first principles. *Phys. Rev. Mater.* **3**, 124003 (2019).
5. Bandurin, D. A. et al. High electron mobility, quantum Hall effect and anomalous optical response in atomically thin InSe. *Nat. Nanotechnol.* **12**, 223–227 (2017).
6. Mudd, G. W. et al. Tuning the Bandgap of Exfoliated InSe Nanosheets by Quantum Confinement. *Adv. Mater.* **25**, 5714–5718 (2013).
7. Zólyomi, V., Drummond, N. D. & Fal'ko, V. I. Band structure and optical transitions in atomic layers of hexagonal gallium chalcogenides. *Phys. Rev. B* **87**, 195403 (2013).
8. Cao, T., Li, Z. & Louie, S. G. Tunable Magnetism and Half-Metallicity in Hole-Doped Monolayer GaSe. *Phys. Rev. Lett.* **114**, 236602 (2015).
9. Zubiaga, A., Garcé, J. A., Plazaola, F., Muñoz-Sanjósé, V. & Martínez-Tomás, C. Near band edge recombination mechanisms in GaTe. *Phys. Rev. B* **68**, 245202 (2003).
10. Antonius, G., Qiu, D. Y. & Louie, S. G. Orbital symmetry and the optical response of single-layer mx monochalcogenides. *Nano Lett.* **18**, 1925–1929 (2018).
11. Pearson, W. B. The crystal structures of semiconductors and a general valence rule. *Acta Crystallogr.* **17**, 1–15 (1964).
12. Gillan, E. G. & Barron, A. R. Chemical Vapor Deposition of Hexagonal Gallium Selenide and Telluride Films from Cubane Precursors: Understanding the Envelope of Molecular Control. *Chem. Mater.* **9**, 3037–3048 (1997).
13. Shangguan, H. et al. Thermoelectric Properties of Two-Dimensional Gallium Telluride. *J. Electr. Mater.* **48**, 5988–5994 (2019).
14. Huang, S. et al. In-Plane Optical Anisotropy of Layered Gallium Telluride. *ACS Nano* **10**, 8964–8972 (2016).
15. Cai, H. et al. Synthesis of Highly Anisotropic Semiconducting GaTe Nanomaterials and Emerging Properties Enabled by Epitaxy. *Adv. Mater.* **29**, 1605551 (2017).
16. Liu, F. et al. High-Sensitivity Photodetectors Based on Multilayer GaTe Flakes. *ACS Nano* **8**, 752–760 (2014).
17. Wang, Z. et al. High-performance flexible photodetectors based on GaTe nanosheets. *Nanoscale* **7**, 7252–7258 (2015).
18. Rhodes, D., Chae, S. H., Ribeiro-Palau, R. & Hone, J. Disorder in van der Waals heterostructures of 2D materials. *Nat. Mater.* **18**, 541–549 (2019).
19. Koma, A. Summary Abstract: Fabrication of ultrathin heterostructures with van der Waals epitaxy. *J. Vacuum Sci. Technol. B: Microelectr. Nanometer Struct.* **3**, 724 (1985).
20. Ehlen, N. et al. Narrow photoluminescence and Raman peaks of epitaxial MoS<sub>2</sub> on graphene/Ir(1 1 1). *2D Materials* **6**, 011006 (2018).
21. Pacuski, W. et al. Narrow Excitonic Lines and Large-Scale Homogeneity of Transition-Metal Dichalcogenide Monolayers Grown by Molecular Beam Epitaxy on Hexagonal Boron Nitride. *Nano Lett.* **20**, 3058–3066 (2020).
22. Yu, Y. et al. Phase-Engineered Synthesis of Ultrathin Hexagonal and Monoclinic GaTe Flakes and Phase Transition Study. *Adv. Funct. Mater.* **29**, 1901012 (2019).
23. Claro, M. S., Grzonka, J., Nicoara, N., Ferreira, P. J. & Sadewasser, S. Wafer-Scale Fabrication of 2D  $\beta$ -In<sub>2</sub>Se<sub>3</sub> Photodetectors. *Adv. Opt. Mater.* **9**, 2001034 (2021).
24. Lee, C. H. et al. Molecular beam epitaxy of 2D-layered gallium selenide on GaN substrates. *J. Appl. Phys.* **121**, 094302 (2017).
25. Chen, M.-W. et al. Large-grain MBE-grown GaSe on GaAs with a Mexican hat-like valence band dispersion. *npj 2D Mater. Appl.* **2**, 2 (2018).



26. Yuan, X. et al. Wafer-scale arrayed p-n junctions based on few-layer epitaxial GaTe. *Nano Res.* **8**, 3332–3341 (2015).
27. Bae, C. J. et al. Influence of thickness on crystallinity in wafer-scale GaTe nanolayers grown by molecular beam epitaxy. *AIP Adv.* **7**, 035113 (2017).
28. Huynh, S. H. et al. Molecular Beam Epitaxy of Two-Dimensional GaTe Nanostructures on GaAs(001) Substrates: Implication for Near-Infrared Photodetection. *ACS Appl. Nano Mater.* **4**, 8913–8921 (2021).
29. Boschker, J. E. et al. Surface reconstruction-induced coincidence lattice formation between two-dimensionally bonded materials and a three-dimensionally bonded substrate. *Nano Lett.* **14**, 3534–3538 (2014).
30. Wang, R. et al. Toward truly single crystalline GeTe films: The relevance of the substrate surface. *J. Phys. Chem. C* **118**, 29724–29730 (2014).
31. Bengió, S., Martin, M., Avila, J., Asensio, M. & Ascolani, H. Atomic structure of the Sb-terminated Si(111) surface: A photoelectron diffraction study. *Phys. Rev. B* **65**, 205326 (2002).
32. Liu, Z. et al. Direct Growth of Graphene/Hexagonal Boron Nitride Stacked Layers. *Nano Lett.* **11**, 2032–2037 (2011).
33. Dau, M. T. et al. Beyond van der Waals Interaction: The Case of MoSe<sub>2</sub> Epitaxially Grown on Few-Layer Graphene. *ACS Nano* **12**, 2319–2331 (2018).
34. Sutter, P. & Sutter, E. Growth Mechanisms of Anisotropic Layered Group IV Chalcogenides on van der Waals Substrates for Energy Conversion Applications. *ACS Appl. Nano Mater.* **1**, 3026–3034 (2018).
35. J. Lopes, J. M. et al. Large-area van der Waals epitaxy and magnetic characterization of Fe<sub>3</sub>GeTe<sub>2</sub> films on graphene. *2D Materials* **8**, 041001 (2021).
36. Klein, A. & Jaegermann, W. Review-Electronic Properties of 2D Layered Chalcogenide Surfaces and Interfaces grown by (quasi) van der Waals Epitaxy. *ECS J. Solid State Sci. Technol.* **9**, 093012 (2020).
37. Wofford, J. M. et al. A hybrid MBE-based growth method for large-area synthesis of stacked hexagonal boron nitride/graphene heterostructures. *Sci. Rep.* **7**, 43644 (2017).
38. Zallo, E. et al. Modulation of van der Waals and classical epitaxy induced by strain at the Si step edges in GeSbTe alloys. *Sci. Rep.* **7**, 1466 (2017).
39. Mortelmans, W. et al. Role of Stronger Interlayer van der Waals Coupling in Twin-Free Molecular Beam Epitaxy of 2D Chalcogenides. *Adv. Mater. Interfaces* **8**, 2100438 (2021).
40. Bandura, A. V., Kovalenko, A. V., Kuruch, D. D. & Evarestov, R. A. Lattice Dynamics and Thermodynamic Properties of Bulk Phases and Monolayers of GaTe and InTe: A Comparison from First-Principles Calculations. *Eur. J. Inorg. Chem.* **2021**, 126–138 (2021).
41. Shenoy, U. S. et al. Electronic structure and properties of layered gallium telluride. *Chem. Phys. Lett.* **651**, 148–154 (2016).
42. Soubelet, P., Bruchhausen, A. E., Fainstein, A., Nogajewski, K. & Faugeras, C. Resonance effects in the Raman scattering of monolayer and few-layer MoSe<sub>2</sub>. *Phys. Rev. B* **93**, 155407 (2016).
43. Zaytseva, Y. S., Borgardt, N. I., Prikhodko, A. S., Zallo, E. & Calarco, R. Electron-Microscopy Studies of the Structure of Thin Epitaxial Ge<sub>2</sub>Sb<sub>2</sub>Te<sub>5</sub> Layers Grown on Si(111) Substrates. *Semiconductors* **55**, 1033–1038 (2021).
44. Hÿtch, M. J., Putaux, J.-L. & Pénisson, J.-M. Measurement of the displacement field of dislocations to 0.03 Å by electron microscopy. *Nature* **423**, 270–273 (2003).
45. Shimizu-Iwayama, T. et al. Visible photoluminescence in Si<sup>+</sup>-implanted silica glass. *J. Appl. Phys.* **75**, 7779–7783 (1994).
46. Schmidt, H. et al. Thermal stability and crystallization kinetics of sputtered amorphous Si<sub>3</sub>N<sub>4</sub> films. *Thin Solid Films* **450**, 346–351 (2004).
47. Mercado, E. et al. Passivation of Layered Gallium Telluride by Double Encapsulation with Graphene. *ACS Omega* **4**, 18002–18010 (2019).
48. Kotha, M., Murray, T., Tuschel, D. & Gallis, S. Study of Oxidation and Polarization-Dependent Optical Properties of Environmentally Stable Layered GaTe Using a Novel Passivation Approach. *Nanomaterials* **9**, 1510 (2019).
49. Stadelmann, P. A. EMS - a software package for electron diffraction analysis and HREM image simulation in materials science. *Ultramicroscopy* **21**, 131–145 (1987).
50. Pozo-Zamudio, O. D. et al. Photoluminescence of two-dimensional GaTe and GaSe films. *2D Mater.* **2**, 035010 (2015).
51. Spindler, C., Galvani, T., Wirtz, L., Rey, G. & Siebentritt, S. Excitation-intensity dependence of shallow and deep-level photoluminescence transitions in semiconductors. *J. Appl. Phys.* **126**, 175703 (2019).
52. Olmos-Asar, J. A., Leão, C. R. & Fazzio, A. Novel III-Te-graphene van der Waals heterojunctions for optoelectronic devices. *RSC Adv.* **7**, 32383–32390 (2017).
53. Wu, Y. et al. Quantum Confinement and Gas Sensing of Mechanically Exfoliated GaSe. *Adv. Mater. Technol.* **2**, 1600197 (2017).
54. Zhao, Q. et al. Thickness-induced structural phase transformation of layered gallium telluride. *Phys. Chem. Chem. Phys.* **18**, 18719–18726 (2016).
55. Ayadi, T., Debbichi, L., Said, M. & Lebègue, S. An ab initio study of the electronic structure of indium and gallium chalcogenide bilayers. *J. Chem. Phys.* **147**, 114701 (2017).
56. Dong, J., Zhang, L., Dai, X. & Ding, F. The epitaxy of 2d materials growth. *Nat Commun.* **11**, 5862 (2020).
57. Arciprete, F. et al. Hints for a General Understanding of the Epitaxial Rules for van der Waals Epitaxy from Ge-Sb-Te Alloys. *Adv. Mater. Interfaces* **9**, 2101556 (2022).
58. Oura, K., Katayama, M., Zotov, A.V., Lifshits, V.G., Saranin, A.A.: Growth of Thin Films. In: Oura, K., Katayama, M., Zotov, A.V., Lifshits, V.G., Saranin, A.A. (eds.) Surface Science: An Introduction. Advanced Texts in Physics, pp. 357–387. Springer, Berlin, Heidelberg (2003). [https://doi.org/10.1007/978-3-662-05179-5\\_14](https://doi.org/10.1007/978-3-662-05179-5_14). Accessed 2022-03-10.
59. Kilaas, R. Optimal and near-optimal filters in high-resolution electron microscopy. *J. Microsc.* **190**, 45–51 (1998).
60. Peters, J.J.P.: Strain++ Software. <https://jjpeters.github.io/Strainpp/>
61. Stukowski, A. Visualization and analysis of atomistic simulation data with OVITO—the Open Visualization Tool. *Model. Simulat. Mater. Sci. Engin.* **18**, 015012 (2010).
62. Krieger, D., Wintersberger, E. & Stangl, J. *xrayutilities*: a versatile tool for reciprocal space conversion of scattering data recorded with linear and area detectors. *J. Appl. Crystallography* **46**, 1162–1170 (2013).
63. Giannozzi, P. et al. Quantum espresso: a modular and open-source software project for quantum simulations of materials. *J. Phys. Condens. Matt.* **21**, 395502 (2009).
64. Perdew, J. P., Burke, K. & Ernzerhof, M. Generalized Gradient Approximation Made Simple. *Phys. Rev. Lett.* **77**, 3865–3868 (1996).
65. Hamada, I. van der Waals density functional made accurate. *Phys. Rev. B* **89**, 121103 (2014).
66. Hamann, D. R. Optimized norm-conserving Vanderbilt pseudopotentials. *Phys. Rev. B* **88**, 085117 (2013).
67. van Setten, M. J. et al. The pseudodojo: Training and grading a 85 element optimized norm-conserving pseudopotential table. *Comput. Phys. Commun.* **226**, 39–54 (2018).
68. Persson, K. Materials Data on GaTe (SG:194) by Materials Project. An optional note (2014). <https://doi.org/10.17188/1184820>.
69. Lazić, P. Cellmatch: Combining two unit cells into a common supercell with minimal strain. *Comput. Phys. Commun.* **197**, 324–334 (2015).

## ACKNOWLEDGEMENTS

The authors would like to thank PDI Berlin for the support with the fabrication and structural characterization of the GaTe samples, M. Hanke and Z. Cheng for the synchrotron based XRD diffraction, C. Stemmler and C. Hermann for their dedicated maintenance of the MBE system, M. Ramsteiner, P. Mazzolini, J.M.J. Lopes, and E. Placidi for fruitful discussions, and P. Moser for help with the PL setup. The work was partly funded by the European Union's Horizon 2020 research and innovation program under Grant Agreement No. 824957 ("BeforeHand": Boosting Performance of Phase Change Devices by Hetero- and Nanostructure Material Design) and by the DFG Priority Programme (SPP 2244) via FI 947/7-1, FI 947/8-1 and KO4005-9/1. CPU time was granted by CINECA through ISCRA C and B initiatives, and by ENEA-CRESCO HPC centers. Measurements were carried out at the U125/2-KMC PHARAO beamline at the BESSY II electron storage ring operated by the Helmholtz-Zentrum Berlin für Materialien und Energie. A.S.P., Y.S.Z. and N.I.B. acknowledge the Ministry of Science and Higher Education of the Russian Federation (State assignment No. FSMR-2023-0003). O.P. acknowledges funding from MUR PRIN2020 "PHOTO". M.P. acknowledges funding from Tor Vergata University TESLA project. O.P. and M.P. acknowledge funding from the EU MSCA-RISE project DiSeTCom (GA 823728) and from INFN TIME2QUEST project.

## AUTHOR CONTRIBUTIONS

E.Z. realized the MBE growth, RHEED, XRD, GID and AFM experiments with help from A.P., S.C., F.A. and R.C. A.S.P., Y.S.Z. and N.I.B. performed TEM experiments. E.Z. carried out Raman and PL spectroscopies with help from M.K., A.P. and J.J.F. A.G., M.P. and O.P. simulated the DFT electronic band structures. E.Z. analyzed the experimental data and wrote the manuscript with input from all authors. All authors reviewed the manuscript. The project was initiated and conceptualized by E.Z. and R.C.

## FUNDING

Open Access funding enabled and organized by Projekt DEAL.

## COMPETING INTERESTS

The authors declare no competing interests.

**ADDITIONAL INFORMATION**

**Supplementary information** The online version contains supplementary material available at <https://doi.org/10.1038/s41699-023-00390-4>.

**Correspondence** and requests for materials should be addressed to Eugenio Zallo.

**Reprints and permission information** is available at <http://www.nature.com/reprints>

**Publisher's note** Springer Nature remains neutral with regard to jurisdictional claims in published maps and institutional affiliations.



**Open Access** This article is licensed under a Creative Commons Attribution 4.0 International License, which permits use, sharing, adaptation, distribution and reproduction in any medium or format, as long as you give appropriate credit to the original author(s) and the source, provide a link to the Creative Commons license, and indicate if changes were made. The images or other third party material in this article are included in the article's Creative Commons license, unless indicated otherwise in a credit line to the material. If material is not included in the article's Creative Commons license and your intended use is not permitted by statutory regulation or exceeds the permitted use, you will need to obtain permission directly from the copyright holder. To view a copy of this license, visit <http://creativecommons.org/licenses/by/4.0/>.

© The Author(s) 2023